

Shuttling a single charge across a one-dimensional array of silicon quantum dots

A. R. Mills,¹ D. M. Zajac,¹ M. J. Gullans,¹ F. J. Schupp,¹ T. M. Hazard,¹ and J. R. Petta¹

¹*Department of Physics, Princeton University, Princeton, New Jersey, USA*

Significant advances have been made towards fault-tolerant operation of silicon spin qubits, with single qubit fidelities exceeding 99.9%¹, several demonstrations of two-qubit gates based on exchange coupling^{2–5}, and the achievement of coherent single spin-photon coupling^{6,7}. Coupling arbitrary pairs of spatially separated qubits in a quantum register poses a significant challenge as most qubit systems are constrained to two dimensions (2D) with nearest neighbor connectivity^{8–10}. For spins in silicon, new methods for quantum state transfer should be developed to achieve connectivity beyond nearest-neighbor exchange^{6,7,11–14}. Here we demonstrate shuttling of a single electron across a linear array of 9 series-coupled Si quantum dots in ~ 50 ns via a series of pairwise interdot charge transfers. By progressively constructing more complex pulse sequences we perform parallel shuttling of 2 and 3 electrons at a time through the 9-dot array. These experiments establish that physical transport of single electrons is feasible in large silicon quantum dot arrays.

Single spin qubits in quantum dots can be fabricated with high areal densities in Si due to their small ~ 30 nm size^{15,16}. In general, electron spins in semiconductors can have spin lifetimes T_1 that approach one minute¹⁷ and coherence times T_2 that exceed one second¹⁸. With single-qubit control fidelities that are competitive with superconducting qubits and trapped ions^{19,20}, and the first realization of high fidelity two-qubit gates^{3,4}, it is becoming increasingly important to now direct attention towards the development of a large-scale and highly-interconnected spin-qubit architecture^{21,22}. Spin qubits in quantum dots are coupled through the exchange interaction at ~ 50 nm length scales^{3,4,23}. Spin-photon coupling was proposed^{11,14,24} as a method for interactions over cm length scales and recently the first experimental advances towards a photonic interconnect have been made^{6,7}. However, the large footprint of the superconducting cavities required for spin-photon coupling motivates the development of intermediate-scale quantum state transfer (QST) protocols that are effective at 50 nm – 10 μ m length scales.

There are many theoretical proposals for achieving intermediate-scale QST in quantum dots. Early work suggested coherent transport by adiabatic passage (CTAP)²⁵ or the implementation

of an exchange coupled “spin-bus”¹². Charges can also be transported in the moving potential of a surface acoustic wave²⁶, through direct shuttling in a gate-voltage induced traveling wave²¹, or by pairwise interdot charge transfers down an array of quantum dots in “bucket brigade” fashion. The bucket brigade approach has been demonstrated in small GaAs quantum dot arrays^{27–29}. However, there are several challenges associated with scaling up the bucket brigade approach. First, for QST of spins, the spin must be transferred on a timescale that is significantly shorter than the inhomogeneous spin dephasing time T_2^* . Second, to allow for adiabatic charge transfer, there must be a substantial 1–5 GHz nearest-neighbor tunnel coupling between all dots in the array. Lastly, the electron transfer process requires a detailed understanding of multidimensional charge stability spaces³⁰ and the ability to precisely navigate through these spaces on nanosecond timescales. Here we demonstrate single charge shuttling using this approach through a linear array consisting of 9 Si quantum dots in ~ 50 ns, more than an order of magnitude faster than $T_2^* \sim 1 \mu\text{s}$ in natural silicon³. Our approach for traversing the high dimensional charge stability space can be extended to larger 1D arrays, and possibly 2D arrays, providing a path towards intermediate-scale QST in silicon.

The experiment is performed using quantum dots defined in an undoped $^{28}\text{Si}/\text{SiGe}$ heterostructure. Lateral confinement of electrons is achieved using a gate design with a repeating unit cell structure consisting of 3 quantum dots and a charge sensor¹⁵. Large 1D quantum dot arrays can be fabricated by repeating the unit cell. Our device is shown in Fig. 1a and consists of 3 unit cells (9 dots and 3 charge sensors). Plunger gates (P_1 , P_2 , etc.) are used to accumulate few-electron quantum dots and barrier gates (B_1 , B_2 , etc.) set the tunnel coupling between the dots. Figure 1b shows a cross-sectional scanning electron microscope image of a gate pattern that is similar to the one used in this experiment. The overlapping nature of the Al gate-electrodes results in a high degree of control over the local electric potential and minimizes capacitive cross-coupling in the device.

The charge shuttling sequence for the 9-dot array is illustrated in Fig. 1c, where the quantum dot confinement potential $V(x)$ is modulated in time by applying voltage pulses to the plunger gates on the device. Starting with an empty array of dots, we load one electron onto dot 1 by lowering its chemical potential below the Fermi level of the source reservoir. The electron is then transferred to dot 2 by lowering its chemical potential while simultaneously increasing the chemical potential of dot 1. We repeat the process of pairwise charge transfers (dot 2 \rightarrow dot 3, dot 3 \rightarrow dot 4, etc.) until the electron resides in dot 9. The charge shuttling sequence is completed by raising the chemical potential of dot 9 above the Fermi level of the drain reservoir, which unloads

the electron from the array. In the absence of shuttling errors, each shuttling cycle will transfer a single electron across the device. Repeating the shuttling process at frequency f will therefore result in a current $I = ef$ through the device.

A high degree of control of charge states in semiconductor double quantum dots (DQDs) has been achieved, as the two-dimensional charge stability diagram that maps out the number of electrons in the left and right dots as a function of the left and right dot gate voltages can easily be measured and visualized³⁰. For the 9-dot linear array, it is not feasible to independently control the electronic occupation of each dot in the array using just two gate voltages. Instead, control over the charge states requires the traversal of a 9D gate voltage parameter space spanned by V_{P1} , V_{P2} , ..., V_{P9} . To simplify the charge shuttling process, we measure the capacitance matrix of the device and use this knowledge to establish “virtual gates” which allow for independent control over the chemical potential of each dot in the array (Supplementary Sec. 1). Through software, the virtual gates largely eliminate the effects of capacitive cross-coupling that would, for example, result in a shift of the dot 2 chemical potential when neighboring plunger gate voltages V_{P1} or V_{P3} are varied. In addition, we break the charge shuttling process down into a sequence of pairwise interdot charge transitions that are executed in virtual gate space. We now describe how the virtual gates are established and utilized to implement charge shuttling through the 9-dot array.

The electrochemical potential $\delta\vec{\mu}$ of the dots is controlled by changing the control gate voltages \vec{V} ^{30,31}. The conversion between \vec{V} and $\delta\vec{\mu}$ is determined by a dimensionless matrix \mathbf{R} related to the capacitance matrix for the device and the experimentally measured dimensionless lever arm for dot 1, $\alpha_1 \approx 0.2$, via the formula $\delta\vec{\mu} = e\alpha_1\mathbf{R}\vec{V}$ (see Fig. 2a and Supplementary Sec. 1). Virtual gates, defined here as u_i , effectively invert the R -matrix, such that a change in u_i only affects the local electrochemical potential of the i^{th} dot, $\delta\mu_i$ (see Fig. 2b). Figures 2c and d illustrate the transition from voltage to virtual gate space. Figure 2c shows the charge stability diagram of a DQD that is formed by accumulating electrons beneath plunger gates P1 and P2 while the rest of the array is fully accumulated to form a channel to the lead. The charge sensor conductance G_{S1} is plotted as a function of the plunger gate voltages V_{P1} and V_{P2} , which change the occupancy (N_1, N_2) of the DQD, where N_i is the number of electrons on dot i . Due to cross-capacitance in the device, a change in V_{P1} results in a slight change in the chemical potential of dot 2. As a result, the dot 1 and 2 charge transitions in Fig. 2c are sloped. By measuring the capacitance matrix of the DQD, it is possible to correct for the cross-capacitance and transform into virtual gate coordinates, where a change in virtual gate parameter u_1 only shifts the chemical potential of dot 1 leaving the chemical potential of the dots in the remainder of the array unchanged. Extraction of the capacitance matrix

from the data in Fig. 2c is detailed in the supplemental text (Supplementary Fig. 2). Figure 2d shows the charge stability diagram of the same DQD, but here plotted as a function of the virtual gate parameters u_1 and u_2 . The dot 1 and dot 2 charge transitions are orthogonal in virtual gate space, allowing for independent control of the chemical potential of each dot.

Larger few electron quantum dot arrays are built up by consecutively adding additional quantum dots to the right side of the device. With a DQD formed from dots 1 and 2, as shown in Fig. 2d, the interdot tunnel coupling t_{c12} is tuned such that $t_{c12} \approx 5 \text{ GHz} \approx 21 \text{ } \mu\text{eV}$ (Supplementary Fig. 4). Dot 3 is then tuned to the $N_3 = 0 \rightarrow 1$ charge transition, as verified in charge sensing. The formation of the third dot slightly affects the capacitance matrix for dots 1 and 2, requiring another calibration to establish the virtual gate space u_1 , u_2 , and u_3 . The tunnel coupling between dots 2 and 3 t_{c23} is then tuned to $t_{c23} \approx 5 \text{ GHz}$. Additional dots are added to the array following the same iterative tuning procedure and tunnel couplings are adjusted as necessary to maintain well-formed dots (Supplementary Fig. 3). To illustrate the formation of a 4 dot array, Figs. 3a–c show pairwise charge stability diagrams that are plotted in virtual gate space for dots 1 and 2 (Fig. 3a), dots 2 and 3 (Fig. 3b), and dots 3 and 4 (Fig. 3c). The remainder of the 9-dot array is configured by simply repeating this tune up procedure.

With a virtual gate space established for the entire device, it is now possible to calculate a shuttling trajectory through the 9-dot charge stability space. For simplicity, the shuttling trajectory is outlined schematically in Figs. 3a–c for the 4-dot configuration (pumping through the 9-dot array is demonstrated in Fig. 4). We initialize the system in the $(0,0,0,0)$ charge state by raising the chemical potentials of dots 1–4 above the Fermi level of the source and drain reservoirs. Here we extend the DQD notation to (N_1, N_2, N_3, N_4) . We then increase u_1 within approximately 1 ns (step I in Fig. 3a) to transfer an electron from the source reservoir onto dot 1, with the device ending up deep in the $(1,0,0,0)$ regime. In step II of Fig. 3a, we move the electron across the $(1,0,0,0)$ – $(0,1,0,0)$ interdot charge transition. This interdot transition, and those that follow, must be performed adiabatically with respect to the interdot tunnel coupling in order to prevent charge pumping errors from occurring (Supplementary Sec. 3). After the interdot charge transition is executed, we move the system deep into the $(0,1,0,0)$ charge regime with the chemical potential of dot 1 brought above the Fermi level of the source reservoir in order to ensure the electron only moves forward in subsequent portions of the shuttling sequence. The $(0,1,0,0)$ – $(0,0,1,0)$ and $(0,0,1,0)$ – $(0,0,0,1)$ interdot charge transitions are crossed in the same way (see steps III and IV in Figs. 3b–c), bringing the electron to dot 4. The final step in the pulse sequence (step V in Fig. 3c) transfers the electron from dot 4 to the drain reservoir and returns the device to the $(0,0,0,0)$

charge state.

It is helpful to visualize the charge shuttling sequence by examining how the potential energy of each dot in the shuttle evolves in time. Figure 3d shows the electrochemical potential $\delta\mu_i$ of each dot induced by the gate electrodes relative to the Fermi level of the source and drain electrodes as a function of time. The units of $\delta\mu_i$ are given as meV/α_1 . The magnitude of the pulses varies from dot to dot due to slight variations in the charging energy across the array. Figure 3e shows energy level diagrams for the 4-dot system at five different instants of time, corresponding to the yellow dots in Figs. 3a–d. The black arrows in Fig. 3e indicate if the chemical potential is increasing or decreasing with time. Note that a conversion from u_i to V_{P_i} is required to program the pulse generator that is used for the pumping sequence (Supplementary Sec. 2).

The four dot charge pumping sequence described in Fig. 3 can be extended to the full 9-dot array by including pulses to execute the interdot transitions associated with dots 4–9. In principle, the pulse sequence can be used for QST of a spin qubit in even larger 1D arrays as long as the total shuttling time is less than T_2^* . To evaluate the performance of the charge shuttle, we measure the current I pumped through the device as a function of the shuttling frequency f . To vary f , we change the dwell time in each charge state, while keeping the ramp rates between charge states fixed. Figure 4c shows I as a function of f for the one electron charge pumping sequence. The pumped current closely follows the expected $I = ef$ relation over the entire range of f explored here. The shuttling direction can be changed by simply reversing the order of the pulse sequence, which yields $I = -ef$.

More complex shuttling trajectories that pump 2 or 3 electrons through the device in parallel can also be executed. These pulse sequences are schematically illustrated in Fig. 4a. For the 2 electron shuttling sequence, the electrons are separated by at least 3 empty dots. The middle panel of Fig. 4a illustrates the $(1,0,0,0,1,0,0,0,0) \rightarrow (0,1,0,0,0,1,0,0,0)$ charge transfer. In the 3 electron shuttling sequence, the electrons are separated by two dots, as illustrated in the right panel of Fig. 4a. The 2 and 3 electron shuttling sequences produce the expected $I = 2ef$ and $I = 3ef$ pumped currents (Fig. 4b). Moreover, as with the 1 electron shuttling sequence, these pulse sequences can be reversed, yielding $I = -2ef$ and $I = -3ef$.

To illustrate the robustness of the 9-dot charge shuttle, Fig. 4c shows the pumped current I as a function of u_1 and u_9 that results from the 3 electron forward shuttling sequence. In contrast to conventional triple point charge pumping, where the pumped current can be a sensitive function of the gate voltages³² we observe a broad plateau of pumped current due to the orthogonality of the virtual gate tuning parameters. While we do not claim that this device will be useful for metrology

applications due to the small magnitude of the pumped current, the 2–3% errors that we observe in the highest pumped currents are entirely consistent with the 3% gain accuracy of the current amplifier used in these measurements. A more precise characterization of the error rate could be performed using single charge detection³³.

In summary, we have shown that we can shuttle individual electrons across an extended 9-dot array using a bucket brigade approach at a rate that is ten times faster than the 1 μ s spin dephasing rate in natural-Si. The shuttling sequence is easily parallelized to simultaneously move up to 3 electrons across the array. Our virtual gate approach for traversing the 9-dimensional charge stability space can be scaled to larger 1D quantum dot arrays, and may also be applicable to 2D arrays, making charge shuttling an attractive candidate as a means of performing intermediate-scale QST within spin-based quantum processors. While this work has demonstrated shuttling of charges through a large $\sim 1 \mu\text{m}$ 1D quantum dot array, it may be extended to examine spin shuttling in Si and the impact of valley states on the spin transfer fidelity²⁹.

-
- ¹ Yoneda, J. *et al.* A quantum-dot spin qubit with coherence limited by charge noise and fidelity higher than 99.9%. *Nat. Nanotech.* **13**, 102 (2018).
- ² Veldhorst, M. *et al.* A two-qubit logic gate in silicon. *Nature* **526**, 410 (2015).
- ³ Zajac, D. M. *et al.* Resonantly driven CNOT gate for electron spins. *Science* **359**, 439 (2018).
- ⁴ Watson, T. F. *et al.* A programmable two-qubit quantum processor in silicon. *Nature* **555**, 633 (2018).
- ⁵ Huang, C.-H., Yang, C. H., Chen, C.-C., Dzurak, A. S. & Goan, H.-S. High-fidelity and robust two-qubit gates for quantum-dot spin qubits in silicon. *arXiv:1806.02858* (2018).
- ⁶ Mi, X. *et al.* A coherent spin-photon interface in silicon. *Nature* **555**, 599 (2018).
- ⁷ Samkharadze, N. *et al.* Strong spin-photon coupling in silicon. *Science* **359**, 1123 (2018).
- ⁸ Linke, N. M. *et al.* Experimental comparison of two quantum computing architectures. *Proc. Natl. Acad. Sci.* **114**, 3305 (2017).
- ⁹ Kandala, A. *et al.* Hardware-efficient variational quantum eigensolver for small molecules and quantum magnets. *Nature* **549**, 242 (2017).
- ¹⁰ Neill, C. *et al.* A blueprint for demonstrating quantum supremacy with superconducting qubits. *Science* **360**, 195 (2018).
- ¹¹ Burkard, G. & Imamoglu, A. Ultra-long-distance interaction between spin qubits. *Phys. Rev. B* **74**, 041307 (2006).
- ¹² Friesen, M., Biswas, A., Hu, X. & Lidar, D. Efficient multiqubit entanglement via a spin bus. *Phys. Rev. Lett.* **98**, 230503 (2007).
- ¹³ Trif, M., Golovach, V. N. & Loss, D. Spin dynamics in InAs nanowire quantum dots coupled to a

- transmission line. *Phys. Rev. B* **77**, 045434 (2008).
- ¹⁴ Hu, X., Liu, Y.-x. & Nori, F. Strong coupling of a spin qubit to a superconducting stripline cavity. *Phys. Rev. B* **86**, 035314 (2012).
- ¹⁵ Zajac, D. M., Hazard, T. M., Mi, X., Nielsen, E. & Petta, J. R. Scalable gate architecture for a one-dimensional array of semiconductor spin qubits. *Phys. Rev. Appl.* **6**, 054013 (2016).
- ¹⁶ Vandersypen, L. M. K. *et al.* Interfacing spin qubits in quantum dots and donors - hot, dense and coherent. *npj Quantum Inf.* **3**, 34 (2017).
- ¹⁷ Camenzind, L. C. *et al.* Hyperfine-phonon spin relaxation in a single-electron GaAs quantum dot. *arXiv:1711.01474* (2017).
- ¹⁸ Tyryshkin, A. M. *et al.* Electron spin coherence exceeding seconds in high-purity silicon. *Nat. Mater.* **11**, 143 (2011).
- ¹⁹ Sheldon, S. *et al.* Characterizing errors on qubit operations via iterative randomized benchmarking. *Phys. Rev. A* **93**, 012301 (2016).
- ²⁰ Harty, T. P. *et al.* High-fidelity preparation, gates, memory, and readout of a trapped-ion quantum bit. *Phys. Rev. Lett.* **113**, 220501 (2014).
- ²¹ Taylor, J. M. *et al.* Fault-tolerant architecture for quantum computation using electrically controlled semiconductor spins. *Nat. Phys.* **1**, 177 (2005).
- ²² Veldhorst, M., Eenink, H. G. J., Yang, C. H. & Dzurak, A. S. Silicon CMOS architecture for a spin-based quantum computer. *Nat. Commun.* **8**, 1766 (2017).
- ²³ Petta, J. R. *et al.* Coherent manipulation of coupled electron spins in semiconductor quantum dots. *Science* **309**, 2180 (2005).
- ²⁴ Petersson, K. D. *et al.* Circuit quantum electrodynamics with a spin qubit. *Nature* **490**, 380 (2012).
- ²⁵ Greentree, A. D., Cole, J. H., Hamilton, A. R. & Hollenberg, L. C. L. Coherent electronic transfer in quantum dot systems using adiabatic passage. *Phys. Rev. B* **70**, 235317 (2004).
- ²⁶ Shilton, J. M. *et al.* High-frequency single-electron transport in a quasi-one-dimensional GaAs channel induced by surface acoustic waves. *J. Phys. Condens. Matter* **8**, L531 (1996).
- ²⁷ Delbecq, M. R. *et al.* Full control of quadruple quantum dot circuit charge states in the single electron regime. *Appl. Phys. Lett.* **104**, 183111 (2014).
- ²⁸ Baart, T. A. *et al.* Single-spin CCD. *Nat. Nanotech.* **11**, 330 (2016).
- ²⁹ Fujita, T. *et al.* Coherent shuttle of electron-spin states. *npj Quantum Inf.* **3**, 22 (2017).
- ³⁰ van der Wiel, W. G. *et al.* Electron transport through double quantum dots. *Rev. Mod. Phys.* **75**, 1 (2002).
- ³¹ Martinis, J. M., Nahum, M. & Jensen, H. D. Metrological accuracy of the electron pump. *Phys. Rev. Lett.* **72**, 904 (1994).
- ³² Roche, B. *et al.* A two-atom electron pump. *Nat. Commun.* **4**, 1581 (2013).
- ³³ Fricke, L. *et al.* Self-referenced single-electron quantized current source. *Phys. Rev. Lett.* **112**, 226803 (2014).

Acknowledgments We thank Lisa Edge for providing the heterostructure used in these experiments. Funded by Army Research Office grant W911NF-15-1-0149, the Gordon and Betty Moore Foundation’s EPiQS Initiative through grant GBMF4535, with partial support from NSF grants DMR-1409556 and DMR-1420541. Devices were fabricated in the Princeton University Quantum Device Nanofabrication Laboratory.

Author contributions A.R.M and D.M.Z carried out the measurements with input from F.J.S. and J.R.P. D.M.Z. fabricated the device. T.M.H. performed early measurements on a different device. M.J.G provided theory support. A.R.M., M.J.G and J.R.P wrote the manuscript. All authors discussed the results and commented on the manuscript.

Correspondence Correspondence and requests for materials should be addressed to J.R.P.

Competing Interests The authors declare that they have no competing financial interests.

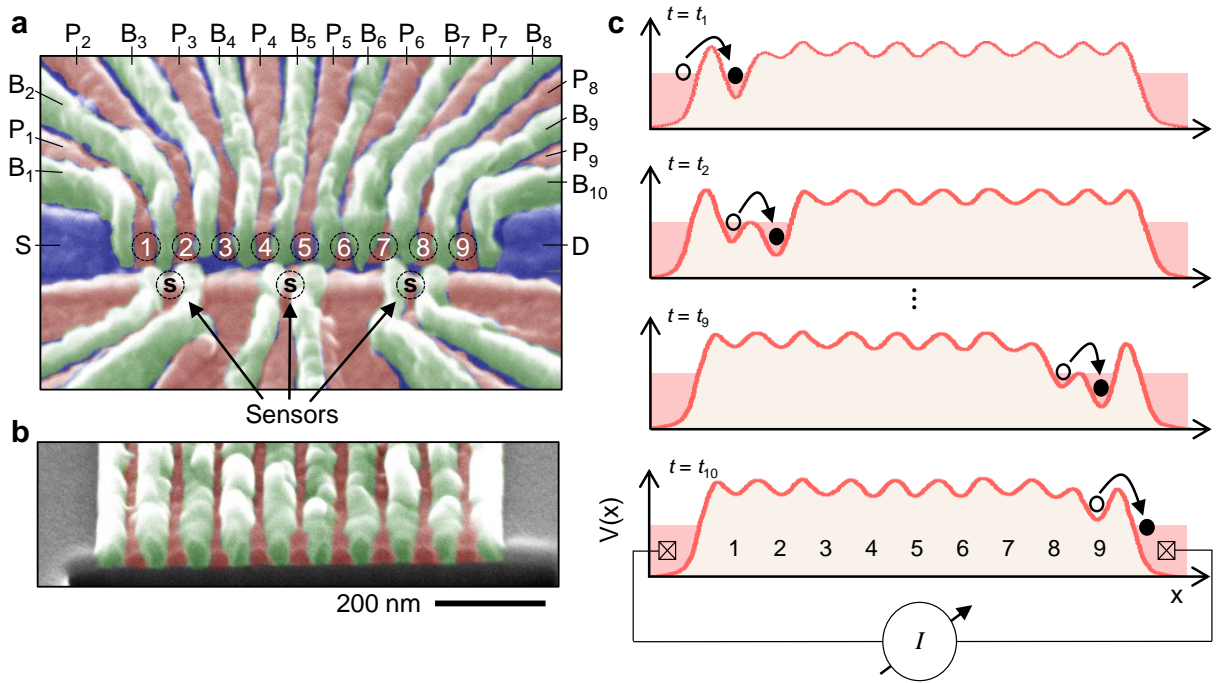


FIG. 1. | **Si charge shuttle** **a**, False-color SEM image of the device consisting of a 9-dot linear array (dots numbered from left to right) with 3 proximal charge sensors (denoted with a circled ‘S’). The potentials of the dots are controlled by the plunger gates (pink) while the tunnel barriers are controlled by the barrier gates (green). The source and drain accumulation gate electrodes are shown in blue. **b**, Tilted-angle cross-sectional SEM image of overlapping Al gates fabricated on a Si substrate. A focused ion beam was used to prepare the sample before imaging. **c**, Illustration of the charge shuttling sequence showing the quantum dot confinement potential $V(x)$ at 4 different times during the shuttling sequence.

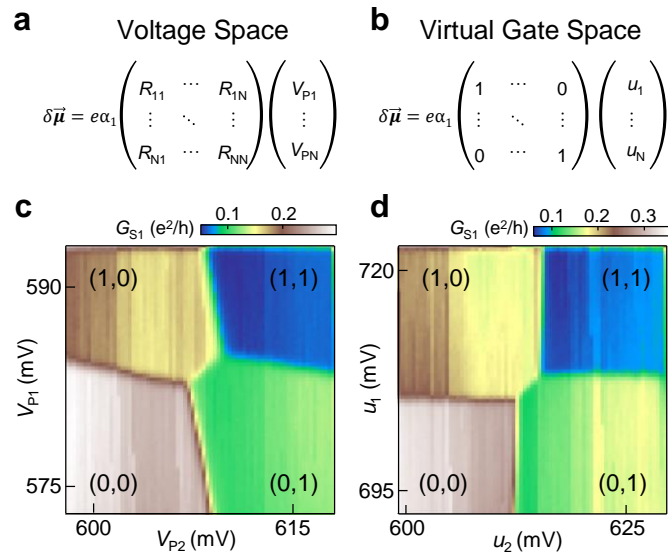


FIG. 2. | **Defining a virtual gate voltage space** The electrochemical potential of the array expressed in gate voltage space **a**, and in virtual gate voltage space **b**. **c**, DQD charge stability diagram for dots 1 and 2, measured as a function of the plunger gate voltages V_{P1} and V_{P2} . **d**, Charge stability diagram for the same DQD, but measured as a function of the virtual gates voltage u_1 and u_2 .

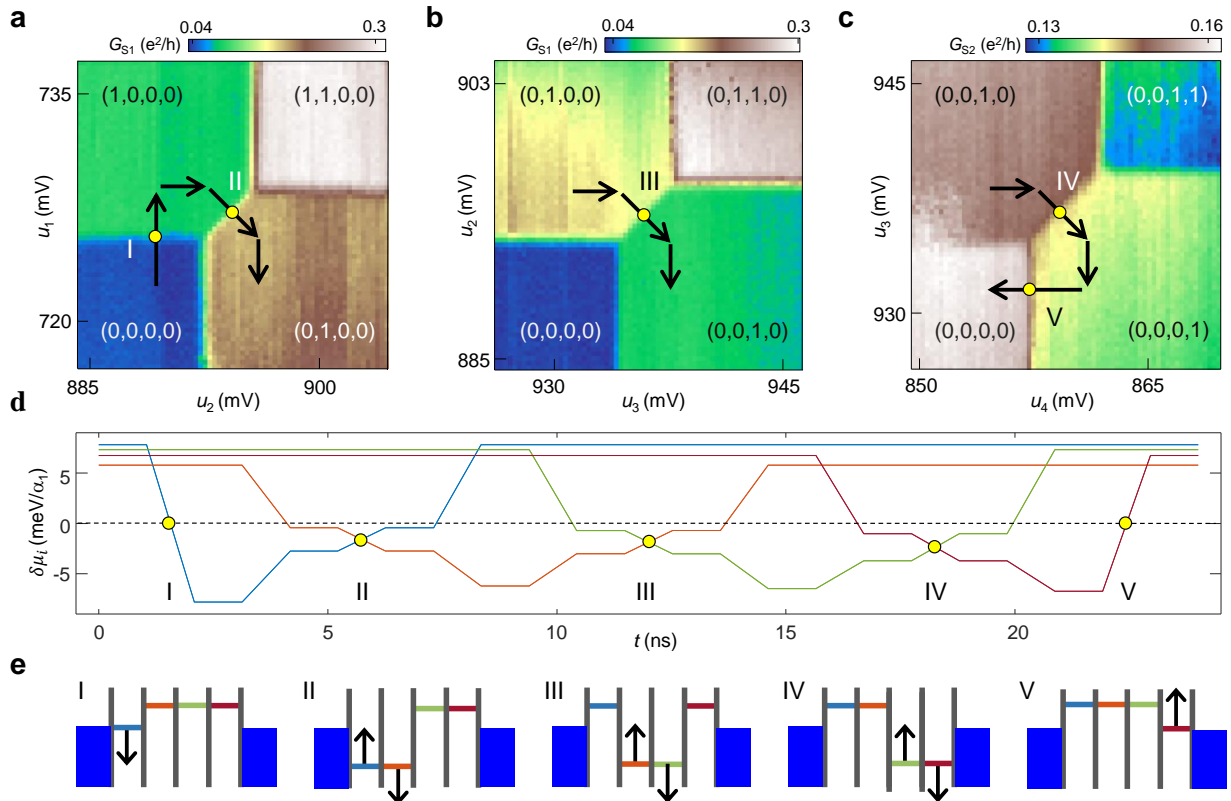


FIG. 3. | **4-dot charge pumping trajectory a-c**, Pairwise charge stability diagrams for dots 1–4, as measured in virtual gate space. The leftmost charge sensor is used to acquire **a** and **b**, while the center charge sensor is used to acquire **c**. The shuttling trajectory through 4-dot charge stability space is overlaid on the data. Different portions of the pulse sequence are labeled with roman numerals for reference in **d** and **e**. **d**, Plot of the electrochemical potential of each dot during the shuttling sequence where the electrochemical potential on dot (1,2,3,4) is plotted in (blue, orange, green, maroon). 1 ns ramp times are used in conjunction with low pass filters so that the interdot charge transfers are adiabatic with respect to interdot tunnel coupling. **e**, Energy level diagrams at the positions in the pulse sequence marked with yellow dots in **a-d** and linked to the corresponding roman numerals. The arrows indicate the direction the energy levels are being swept and the colors of the levels correspond to the colors of the pulses in **d**.

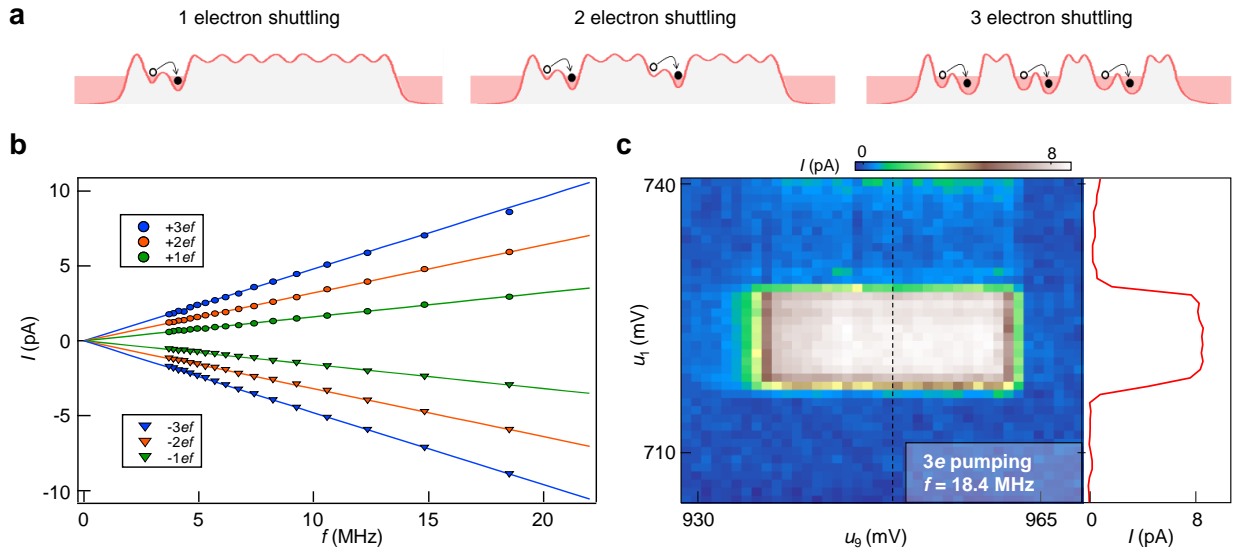


FIG. 4. | **9-dot charge shuttling** **a**, Examples of single, double, and triple electron charge shuttling sequences. **b**, Current I measured as a function of frequency f for single, double, and triple electron charge shuttling in both the forward and reverse directions. For reference, the solid line shows the expected current $I = nef$ for $-3 \leq n \leq 3$. **c**, I measured as a function of u_1 and u_9 during continuous 3-electron charge shuttling. A robust region of pumped current is observed. Right panel: A line-cut through the data shows a stable plateau of pumped current.